JPhys Energy

PAPER • OPEN ACCESS

$Mg_xZn_{1-x}O$ contact to $CuGa_3Se_5$ absorber for photovoltaic and photoelectrochemical devices

To cite this article: Imran S Khan *et al* 2021 *J. Phys. Energy* **3** 024001

Journal of Physics: Energy

OPEN ACCESS

RECEIVED
7 October 2020

REVISED
9 December 2020

ACCEPTED FOR PUBLICATION
15 December 2020

PUBLISHED
28 January 2021

PAPER

$Mg_xZn_{1-x}O$ contact to $CuGa_3Se_5$ absorber for photovoltaic and photoelectrochemical devices

Imran S Khan[1], Christopher P Muzzillo[1], Craig L Perkins[1], Andrew G Norman[1], James L Young[1], Nicolas Gaillard[2] and Andriy Zakutayev[1]

[1] National Renewable Energy Laboratory, Golden, CO, USA
[2] Hawaii Natural Energy Institute, University of Hawaii, Honolulu, HI, USA

E-mail: andriy.zakutayev@nrel.gov

Keywords: photovoltaic device, photoelectrochemical device, CuGa3Se5, MgZnO

Supplementary material for this article is available online

Abstract

$CuGa_3Se_5$ is a promising candidate material with wide band gap for top cells in tandem photovoltaic and photoelectrochemical (PEC) devices. However, traditional CdS contact layers used with other chalcopyrite absorbers are not suitable for $CuGa_3Se_5$ due to the higher position of its conduction band (CB) minimum. $Mg_xZn_{1-x}O$ (MZO) is a transparent oxide with adjustable band gap and CB position as a function of magnesium composition, but its direct application is hindered by $CuGa_3Se_5$ surface oxidation. Here, MZO is investigated as a contact (n-type 'buffer' or 'window') material to $CuGa_3Se_5$ absorbers pretreated in Cd^{2+} solution, and an onset potential close to 1 V vs reversible hydrogen electrode in 10 mM hexaammineruthenium (III) chloride electrolyte is demonstrated. The Cd^{2+} surface treatment changes the chemical composition and electronic structure of the $CuGa_3Se_5$ surface, as demonstrated by photoelectron spectroscopy measurements. The performance of $CuGa_3Se_5$ absorber with Cd^{2+} treated surface in the solid-state test structure depends on the Zn/Mg ratio in the MZO layer. The measured open circuit voltage of 925 mV is promising for tandem PEC water splitting with $CuGa_3Se_5$/MZO top cells.

1. Introduction

Hydrogen is considered one of the most promising means of storing renewable energy because it is the most abundant element in the world, has the highest energy density among non-nuclear fuels, and is a zero-emission fuel [1]. Solar photoelectrochemical (PEC) water splitting can be used to produce hydrogen, but a commercially viable PEC device technology remains elusive despite long research history [2]. Tandem monolithic PEC devices with a multijunction hybrid photoelectrode [3] consisting of group III–V semiconductors have been able to reach direct water splitting solar-to-hydrogen (STH) efficiency above 19% [4]. However, large scale commercial adoption of such technology is limited by high processing costs and finite durability during PEC water splitting. To maintain high efficiency and reduce processing cost, tandem PEC devices with chalcopyrite absorber materials can be adopted from photovoltaic (PV) research. These chalcopyrites have lower deposition cost and higher defect tolerance, which together with bandgap tunability makes them attractive for application in solar water splitting. Indeed, wide bandgap chalcopyrite $CuGaSe_2$ [5, 6], $(Ag,Cu)GaSe_2$ [7, 8], $CuGa(S,Se)_2$ [9] and $Cu(In,Ga)S_2$ [10] photocathodes have shown promising PEC performance and stability, and emerging wide bandgap $CuGa_3Se_5$ has been recently proposed [11].

$CuGa_3Se_5$ is an ordered-vacancy compound derived from the chalcopyrite structure of the well-known $CuGaSe_2$ absorber material by substituting Ga at Cu sites and leaving Cu sites vacant, $[2V_{Cu}^{-1} + Ga_{Cu}^{+2}]$ [12]. Reducing the Cu/Ga composition widens the band gap by reducing the valence band energy by ~0.2 eV, because of lower contribution from the Cu 3d states to the valence bands [13]. Due to its ideal bandgap of 1.84 eV and suitable conduction band (CB) alignment for H_2 evolution, $CuGa_3Se_5$ is a promising absorber material candidate for top cell applications in tandem PEC water splitting devices. Calculations show that if paired with a 1.23 eV bandgap absorber in a tandem PEC cell, $CuGa_3Se_5$ could potentially lead to STH

efficiency as high as 22.8% [14]. Initially a $CuGa_3Se_5$/ZnS/Pt device with current output of 8 mA cm^{-2} (0 V vs RHE, 3-electrode) was reported [15], and subsequently the photocurrent density was increased up to 9.3 mA cm^{-2} for a mixed phase of $CuGaSe_2$ and $CuGa_3Se_5$ with CdS-modified surface and Pt catalyst [16]. More recently, 17 d of continuous water splitting operation for a bare $CuGa_3Se_5$ absorber photocathode with ~12 mA cm^{-2} photocurrent at −1 V vs RHE have been demonstrated by our team, suggesting promising durability [11]. These encouraging outcomes clearly point out the need for further fundamental study of this absorber and its interface with other materials.

Traditional chalcopyrites $CuGaSe_2$ and ordered-vacancy $CuGa_3Se_5$ absorbers are often interfaced with CdS as a contact material (also known as n-type 'buffer' or 'window') to create the p–n junction. However, CdS contact layers suffer from short wavelength absorption and instability in electrolyte solution. In addition, CdS has a cliff-like ~0.2 eV CB offset with stoichiometric $CuGaSe_2$, and a similar CB offset is expected for $CuGa_3Se_5$ [17]. If the conduction band minimum (CBM) of the contact is lower than that of the absorber (a 'cliff' type offset), the device suffers from lower photovoltage, increased interface recombination, and other detrimental effect to device performance [18–20]. If a CBM of the contact is more than 0.3 eV above that of the absorber (a 'spike' type offset), the resulting barrier impedes the collection of photo-generated carriers [21–23].

To address these challenges, $Mg_xZn_{1-x}O$ (MZO) [24, 25] with tunable CB position as a function of Mg content has been proposed as an attractive n-type contact layer. MZO thin film was demonstrated with up to $x = 0.46$ grown by radio frequency (RF) co-sputtering without any phase segregation resulting in a bandgap of up to 4.2 eV, while ZnO has a bandgap of 3.24 eV [24]. Combinatorial studies explored the composition spreads of MZO with different deposition methods, such as pulsed laser deposition [26, 27] and chemical vapor deposition [28]. In a previous combinatorial study, we showed that the CB position could be tuned by 0.5 eV as Mg concentration changes from 4% to 12% [29], suggesting that it might be a suitable contact to $CuGa_3Se_5$ absorber. Integration of MZO as contact material resulted in significant efficiency improvements in different solar cell device technologies such as CdTe [30] and CIGS [31, 32], as well as $CuGaSe_2$ [33] that likely has similar CB position to $CuGa_3Se_5$.

In this study, MZO was investigated as the contact layer material for $CuGa_3Se_5$ absorber-based PV and PEC devices. Structural, optical and electrical properties of MZO thin films were studied as a function of different experimental conditions such as Mg composition, Ga doping, substrate temperature and deposition ambient. MZO depositions were performed by combinatorial RF sputtering. For functional $CuGa_3Se_5$/MZO PV device, absorber surface pretreatment with Cd^{2+} solution was crucial because it removed surface oxidation, led to Cd incorporation, and possibly changed the surface conductivity type. MZO deposition and the surface pretreatment conditions were optimized for solid state solar cell performance. The outcome was a significant improvement in open circuit voltage (up to 920 mV) compared to conventional CdS-contact $CuGa_3Se_5$ devices (~730 mV). Replacement of CdS also improved quantum efficiency (QE) in the blue region of the spectrum. The PEC characteristics of $CuGa_3Se_5$/MZO as photocathode are tested with hexaammineruthenium (III) chloride sacrificial redox electrolyte, which exhibited an onset potential near 1 V vs RHE. These outcomes indicate that $CuGa_3Se_5$/MZO could serve as an efficient top cell for tandem PV and PEC water splitting devices.

2. Experimental methods

2.1. Material synthesis and measurements

Ga-doped MZO thin film sample libraries with orthogonal composition gradients of Mg and Ga were deposited by combinatorial RF magnetron sputtering from ZnO, Mg and Ga_2O_3 targets (figure 1(a)). 50 × 50 mm Eagle XG glass substrates were cleaned with laboratory grade detergent followed by sonication in warm deionized water, acetone and isopropanol. MZO depositions were done at a pressure of 3 mTorr in Ar/O_2 atmosphere where the total gas flow rate was fixed at 16 sccm. The chamber base pressure was 5×10^{-7} Torr. O_2 flow, found to be crucial for good quality transparent films, was varied from 0.5% to 2% of the total gas flow for different depositions. A premixed 5% O_2 in Ar cylinder was used as O_2 source for precise flow control. A gas ring around the substrate carrying the O_2 lines ensured uniform O_2 containing environment across the substrate. The samples were mounted on a temperature calibrated Inconel substrate holder and heated by a radiative heater. The substrate temperature was varied from room temperature to 200 °C. The depositions were performed for 120 min, that resulted in film thicknesses in the 80–120 nm range.

Each sample was characterized at 4 × 11 grid points with the following spatially resolved methods (figure 1(b)). X-ray diffraction (XRD) patterns for the MZO thin films were obtained using a Bruker D8 Discover XRD instrument. Electrical resistivity/conductivity data was measured by a custom four-point probe system; the highest measurable sheet resistance by the equipment is ~5×10^7 $\Omega\,\square^{-1}$. Optical

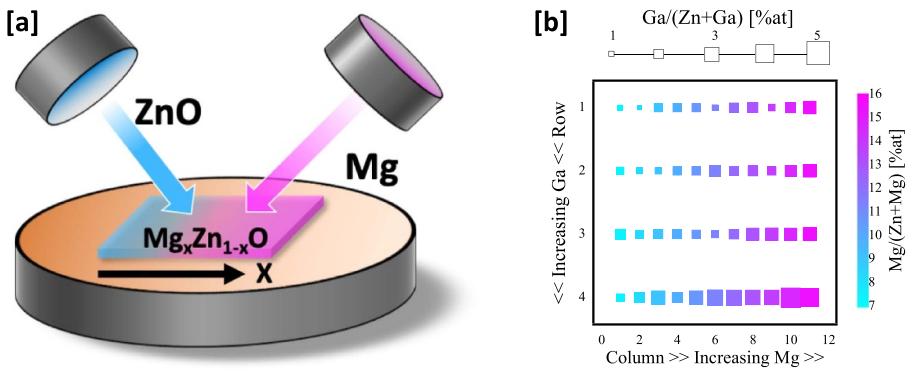

Figure 1. (a) Combinatorial sputter deposition of $Mg_xZn_{1-x}O$ thin films. (b) 4 × 11 composition measurement grid for Ga:$Mg_xZn_{1-x}O$ films on a 50 × 50 mm glass substrate.

absorption was measured with a custom UV/Vis/NIR Spectroscopy system equipped with an OceanOptics DH-2000-BAL deuterium-halogen light source and a StellerNet EPP2000-UVN-SR spectrometer.
The chemical compositions of the films, atomic Ga/(Ga + Zn) ratio, were measured with a Fisherscope XUV-733 x-ray fluorescence (XRF) instrument. Mg, being a light element, was quantified using Rutherford backscattering spectroscopy (RBS) and energy dispersive x-ray spectrometry (EDX). EDX data was taken using an acceleration voltage of 5.0 keV. For Mg quantification purpose, 10 × 10 mm glassy carbon or silicon witness substrates were placed at the 2nd row of the 4 × 11 sample library grid. The use of such impurity free witness substrates reduced background noise in quantification of light elements in small amounts.
Mg composition in the PV device library was estimated from an identical condition MZO deposition on a glass substrate. The measurements with a Bruker M4 Tornado XRF instrument were calibrated using the Mg composition measured by EDX on Si witness substrates. Experimental combinatorial data collected in this study were managed, analyzed and displayed using our publicly available COMBIgor software package for Igor Pro [34], and will be made available through the High Throughput Experimental Materials Database [35].

Kelvin probe measurement system from KP technology was used to determine the work function for both the MZO (on doped Si substrates) and $CuGa_3Se_5$ (on Mo coated glass substrates) films. A gold reference (work function 5.1 eV) in air was used to quantify the absolute value of the surface potentials. X-ray photoelectron spectroscopy (XPS) was performed on the $CuGa_3Se_5$ films using monochromatic Al Kα radiation and a pass energy of 29 eV. The spectrometer binding energy scale was calibrated at high and low energy using clean gold and copper foils and known transition energies. Data analysis and peak fitting were performed using a combination of Igor and PHI MultiPak.

Cross-section scanning electron microscopy (SEM) image of the device was taken with a Hitachi S-4800 SEM instrument operated at 2 kV. Cross-section transmission electron microscopy (TEM) specimens were prepared using the focused ion beam (FIB) lift out technique with the final Ga^+ ion milling performed at 3 kV. Ga^+ ion FIB damage was subsequently removed using low energy (<1 kV) Ar^+ ion milling in a Fischione Nanomill with the sample cooled by liquid nitrogen. Scanning transmission electron microscopy (STEM) imaging, high-angle annular dark-field (HAADF) imaging and EDX mapping analysis were performed in a FEI Tecnai F20 UltraTwin field emitting gun STEM operated at 200 kV and equipped with an EDAX Octane T Optima Si drift detector EDX system.

2.2. Device fabrication and characterization

Substrates for device fabrication were soda-lime glass. Mo back contact was deposited by Direct Current sputtering. Near stoichiometric $CuGa_3Se_5$ thin films with Cu/Ga = 0.36 composition were deposited by three-stage co-evaporation (Ga-Se in the 1st stage, Cu-Se in the 2nd stage, and Ga-Se in the 3rd stage) at 600 °C. For comparison, a baseline device was fabricated in a similar fashion to narrow bandgap (∼1.1 eV) CIGS absorber devices, more details on the process steps can be found elsewhere [11, 36]. The solution for Cd^{2+} surface treatment contained 2 mM $CdSO_4$ in NH_4OH and DI water, and no S precursor. For the XPS/UPS, Kelvin Probe, SEM, STEM, EDX and PEC measurements on Cd^{2+} treated $CuGa_3Se_5$ absorbers the treatment temperature was 65 °C, while for PV devices different temperatures were investigated. Only device data containing undoped MZO is presented here, as they produced superior devices.

PEC characteristics of the devices were measured by performing chopped-light linear sweep voltammograms (LSV) in a three-electrode configuration with $CuGa_3Se_5$ photocathode, Pt counter

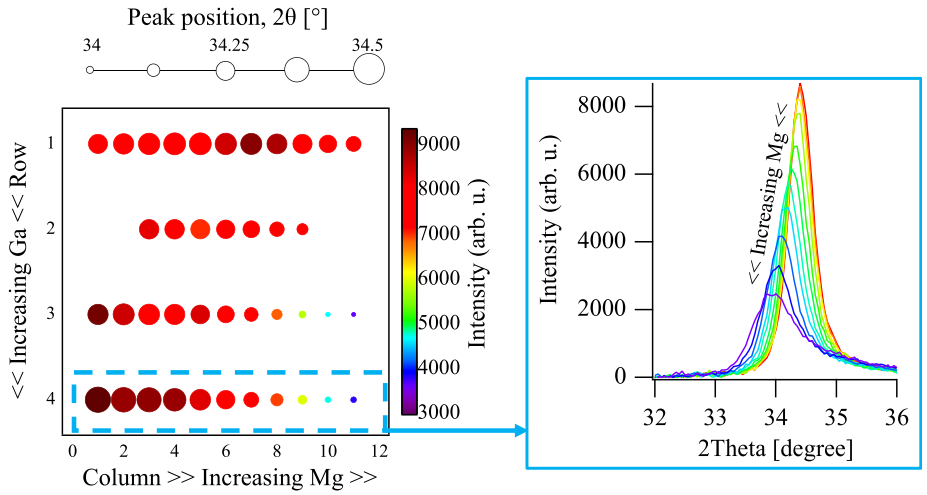

Figure 2. ZnO (0002) peak position and intensity for a Ga:$Mg_xZn_{1-x}O$ sample library deposited at 200 °C.

electrode, and Ag/AgCl reference electrode with 3 M NaCl filling solution. Photoelectrodes were made by indium bonding an insulated Cu wire to an exposed part of the Glass/Mo substrate. A number of different electrolyte solutions was tested, including (1 M Na_2SO_4 + pH7 buffer), (NaOH + H_2SO_4 + 0.5 M Na_2CO_3, pH = 9.6), and (0.5 M Na_2SO_4 + 0.25 M KH_2PO_4 + 0.25 M K_2HPO_4, pH = 6.7), yet the $CuGa_3Se_5$/MZO thin films were found to be unstable in all of these solutions with the photocurrent limited due to charge transport. As such, LSV analyses were performed in a solution containing 10 mM hexaammineruthenium (III) chloride, 0.5 M KCl and pH7 buffer. During the measurements, the samples were illuminated with a 300 W Xenon arc lamp (Newport) through an AM 1.5G filter (Oriel), simulating one-sun equivalent illumination as adjusted using a calibrated 1.8 eV $GaInP_2$ PV reference cell. The electrode device area was defined by nonconductive epoxy (Loctite 9462), which isolated the wire and Mo substrate from the electrolyte. The device areas were measured by counting the number of pixels from digitally scanned images of the electrodes. Potentials are reported against the RHE by using the relationship $E(\mathrm{RHE}) = E_{\mathrm{Ag/AgCl}} + 0.059 \times \mathrm{pH} + E_{\mathrm{o,Ag/AgCl}}$, where $E_{\mathrm{o,Ag/AgCl}} = 0.209$ V. The standard reduction potential (E_o) for the hexaammineruthenium redox couple is 0.1 V vs RHE [37].

For PV device fabrication, Al:ZnO (120 nm) as transparent conductive oxide was deposited by RF magnetron sputtering, and Ni (50 nm)/Al (3 μm) front grids by e-beam evaporation [36]. Solar cell performance was characterized based on photocurrent density–voltage (JV) and QE performances. JV data for the combinatorial device library was collected with a custom made automated XY probe station under AM1.5 light from an Oriel 91194-1000 solar simulator with the samples maintained at 20 °C. External QE for select devices were measured with a Newport Oriel IQE-200.

3. Results and discussions

3.1. $Mg_xZn_{1-x}O$ thin film characterization

For $CuGa_3Se_5$ device integration, combinatorial RF sputtered MZO was deposited with x values in the 0–0.15 range, and Ga/(Ga + Zn) atomic ratio from 0% to 15%. Figure 1(b) shows the composition profile of one such Ga:MZO library, and RBS data for a selected sample is presented in figure S1 (available online at stacks.iop.org/JPENERGY/3/024001/mmedia). XRD patterns of the MZO films were all (0002) oriented wurtzite ZnO; no peaks related to MgO or Ga_2O_3 secondary phases were observed for the investigated span of Mg and Ga compositions (figure 2). With increasing Mg composition, the ZnO (0002) peak broadened, intensity reduced and shifted towards lower angles. This shift was more significant at higher Ga/(Ga + Zn) samples. Mg atomic size is much lower than Zn or Ga. Mg incorporation at large degree could induce strain in the ZnO crystal, indicated by the peak broadening at high Mg samples.

The film conductivity for the undoped MZO films deposited at 100 °C or below were too low to be measured. The conductivity for the doped MZO films were dependent on Ga and Mg compositions (figure 3(a)). Conductivity decreased with increasing Mg composition, possibly due to wider bandgap and increased carrier scattering. Introduction of Ga as dopant increased conductivity, and then decreased it at higher Ga concentrations when Ga/(Ga + Zn) atomic ratio exceeded 5%. This was likely due to the reduced crystallinity of those samples, as evident from the XRD data. The highest conductivity was 20 S cm^{-1} and

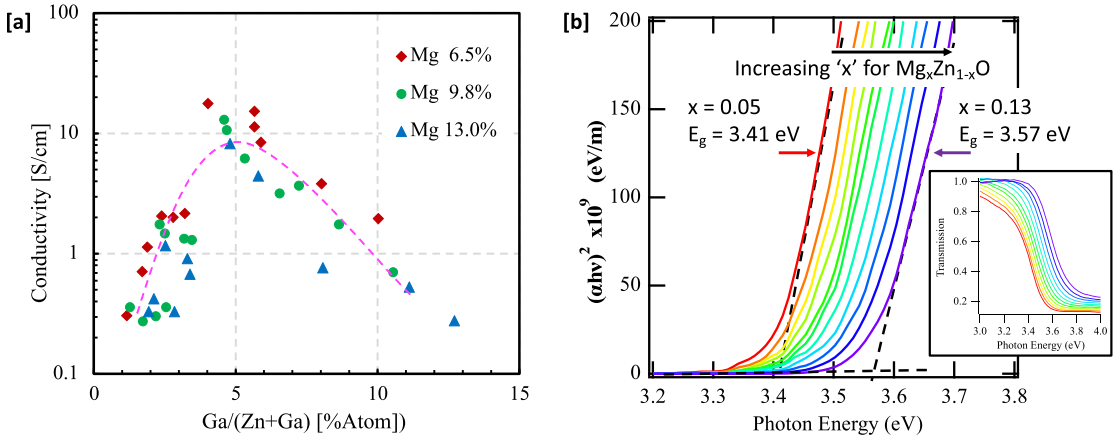

Figure 3. (a) Conductivity vs Ga/(Ga + Zn) atomic ratio for $Mg_xZn_{1-x}O$:Ga thin films deposited at 200 °C. (b) Tauc plot from the transmittance data showing the shift in the estimated optical bandgap for undoped MZO films with increasing Mg composition.

Table 1. Photocurrent onset potentials and photovoltages from the LSV data.

Electrode	V_{onset} (V vs RHE)	Photovoltage (V)
$CuGa_3Se_5$ (as deposited)	0.57 ± 0.02	0.47 ± 0.02
$CuGa_3Se_5/(Cd^{2+})$	0.64 ± 0.02	0.54 ± 0.02
$CuGa_3Se_5$/CdS/i-ZnO	1.18 ± 0.04	1.08 ± 0.04
$CuGa_3Se_5/(Cd^{2+})$/i-MZO	1.08 ± 0.03	0.98 ± 0.03

was observed at Ga/(Ga + Zn) value of 4%. Mg incorporation also resulted in the expected bandgap widening. Increasing Mg composition increased the optical bandgap of MZO, calculated from the Tauc plot of the absorption data from UV–Vis spectroscopy (figure 3(b)). For the highest experimented Mg composition of 13%, optical band gap values up to 3.57 eV was estimated.

3.2. Photoelectrochemical characteristics

The PEC characteristics of the $CuGa_3Se_5$ photocathodes were investigated with chopped light linear sweep voltammetry (LSV) with a three-electrode system under simulated AM1.5G illumination. The LSV data is shown in supplement figure S2, for analysis performed in hexaammineruthenium (III) chloride redox mediator and KCl supporting electrolyte with pH7 buffer. It should be noted that LSV measurement performed with a sacrificial redox agent is not water splitting, however it gives an estimate of the quality of the device characteristics. In the light, the measured photovoltage is relative to the reaction potential of hexaammineruthenium (III) chloride redox mediator, which is 0.10 V vs RHE [37]. Thus, the photovoltage is the difference between photocurrent onset potential and redox couple potential for each measurement. The photocurrent onset potentials and photovoltages obtained from the LSV curves of figure S2 are shown in table 1. There was sign of degradation during consecutive testing, however that could be due to scanning near high anodic potentials. The dark current was nearly zero. The photocurrent saturated at more cathodic potentials. The initial current transient could be due to charge transport limitation in the electrolyte and/or at the electrode surface.

The untreated Mo/$CuGa_3Se_5$ electrode had a photocurrent onset potential (V_{onset}) of ~0.57 V vs RHE. The Fermi level of the p-type $CuGa_3Se_5$ semiconductor would be located much lower than the solution potential (reduction potential of the redox). This would create a charge depletion layer in the semiconductor due to transfer of valence band hole to the solution. In equilibrium, this charge separation would form a built-in electric field, causing a downward band bending. The potential V_{onset} is indicative of this built-in potential. An increase of V_{onset} up to 0.64 V vs RHE, for Cd^{2+} solution treated $CuGa_3Se_5$ electrode indicated an increase of this band bending.

For $CuGa_3Se_5$/n-CdS/i-ZnO device, V_{onset} close to 1.2 V vs RHE was observed. This was indicative of the good interface passivation and/or extended depletion region due to increased band bending at the p–n junction formed between n-CdS and p-$CuGa_3Se_5$. The optimized $CuGa_3Se_5/(Cd^{2+})$/MZO devices also exhibited V_{onset} potential near 1.0 V vs RHE. However, this value for devices with Cd^{2+} treated absorber surfaces was lower compared to baseline CdS devices, possibly due to the lack of an active n-type layer. This difference in the onset potential could not be due to substitution of MZO for i-ZnO alone, since $CuGa_3Se_5$/MZO solid-state stacks resulted in no photo-response. Even with the absence of an evident active

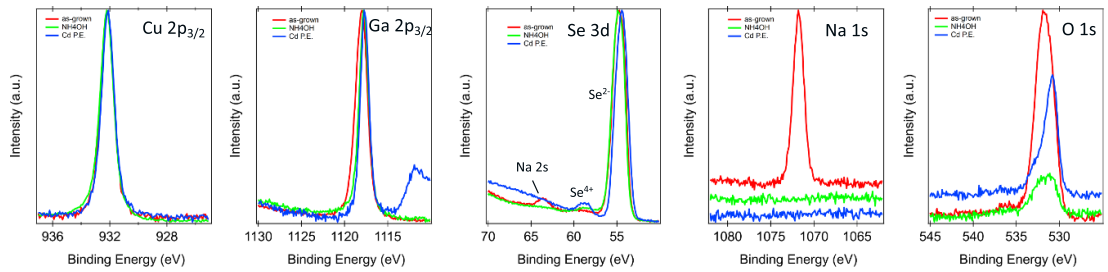

Figure 4. Elemental core levels of the $CuGa_3Se_5$ surface with different surface treatments, measured by XPS.

Table 2. XPS, XRF and EDX elemental composition of untreated and treated $CuGa_3Se_5$ absorber.

$CuGa_3Se_5$	Technique	O (%)	Na (%)	Cu (%)	Ga (%)	Se (%)	Cd (%)
As deposited	XPS	41.8	7.9	3.4	24.5	22.5	—
		(normalized)		6.7	48.6	44.7	—
	XRF		—	11.2	32.5	55.6	—
	EDS	—	—	14.2	45.1	40.7	—
NH_4OH treatment	XPS	10.9	—	18.4	25.1	45.7	—
		(normalized)		20.6	28.1	51.3	—
Cd^{2+} treatment 65 °C	XPS	21.2	—	4.8	19.8	35.8	18.4
		(normalized)		8.0	32.7	59.3	—

n-type layer, the $CuGa_3Se_5/(Cd^{2+})$/MZO devices still exhibited V_{onset} potential above 1 V vs RHE. This encouraging result indicated that Cd^{2+} treatment itself introduced a surface passivation and/or a band bending at the absorber interface. However, for (Cd^{2+})-MZO (undoped) modified electrode the band bending must be lower compared to the CdS modified electrode, evident form the onset potential values. A schematic of the equilibrium band diagram for a $CuGa_3Se_5$/MZO photoelectrode is shown in the supplement figure S2 inset.

3.3. Surface and interface

To better understand the PEC characteristics of the electrodes, the absorber surface and interface modification due to the Cd^{2+} solution treatment was further investigated. Surface sensitive XPS/UPS of the as-deposited and treated $CuGa_3Se_5$ revealed how the wet treatment affected the absorber surface (figure 4). The XPS survey spectrum of the as-deposited $CuGa_3Se_5$ is shown in the supplement figure S3. The surface doping of as grown $CuGa_3Se_5$ appeared stable over a period of months, and was only slightly p-type (the XPS measurement on the as grown sample was repeated after 3 months, data not shown). The valence band position ($E_F - E_{VBM}$) value measured with monochromatic Al K_α and He I excitation was 0.55 eV and 0.72 eV respectively (supplement figure S4). UPS results with He I light (21.2 eV) had a probe depth of less than 1 nm in the sample surface, while VBM measurements with Al K_α (1487 eV) measured up to 10 nm into the bulk of the film due to higher photoelectron kinetic energy. This indicated the presence of a downward band bending at the as-grown surface.

The elemental compositions of the $CuGa_3Se_5$ surface with different treatments is shown in table 2. There were a number of changes that happened with both NH_4OH and Cd^{2+} (65 °C 15 min) treatments (figure 4). A high degree of surface oxidation is observed for as deposited absorber, along with Na diffused from the soda lime glass substrate. With both NH_4OH and Cd^{2+} treatments, surface Na was removed and the O quantity was reduced. The gallium $2p_{3/2}$ peak narrowed significantly with Cd^{2+} treatment, probably due to the removal of gallium oxides. It is also interesting to note that the cadmium solution treatment (and likely the subsequent air exposure), caused the appearance of oxidized selenium, Se^{4+}. For CdTe devices a very thin layer of oxidized tellurium was found to be critical for well-passivated interfaces [38]. Such Se oxidation could also be beneficial for surface passivation of the $CuGa_3Se_5$ absorbers studied here.

No Cd could be detected on the Cd^{2+} treated $CuGa_3Se_5$ films using XRF and SEM/EDX analysis techniques, which are more sensitive to the bulk than XPS. Such comparison of XPS and EDX (probes deeper, up to 100 nm) and XRF (probes up to 1000 nm) compositions for as-grown films indicated a Cu deficiency on the surface which is likely due to the sites being replaced by Na atoms. Cd^{2+} treatment introduced Cd on the absorber surface (supplement figure S3). Exposure of the surface to aqueous cadmium sulfate likely caused an ion exchange process between cadmium and copper. Removal of Na atoms by NH_4OH could allow Cd atoms to occupy these sites and change surface doping. The ($E_F - E_{VBM}$) values from

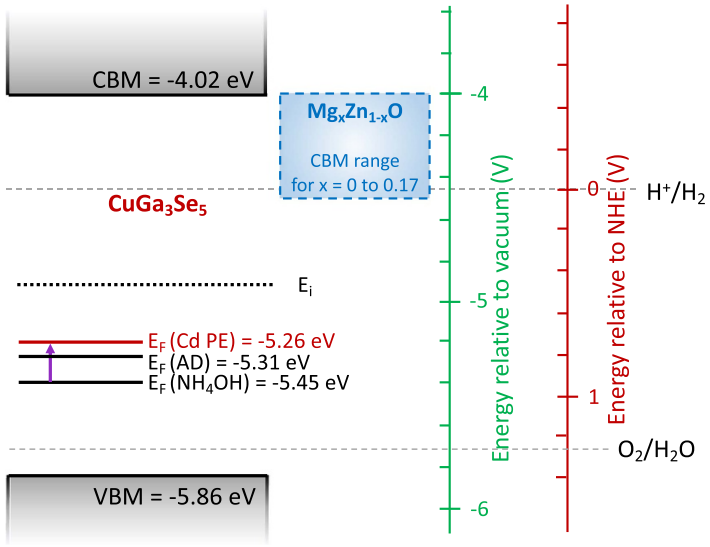

Figure 5. Energy band positions for $CuGa_3Se_5$ absorber with different surface treatments, in comparison with the CBM position in $Mg_xZn_{1-x}O$.

XPS and work function values from Kelvin probe measurement for differently treated films also suggested a change in surface doping.

Figure 5 shows the band diagram for $CuGa_3Se_5$ with Fermi energy level (E_F) positions for different treatments. The E_F values with respect to valence band maximum (E_{VBM}) are derived from XPS measurements. The change in E_F with different surface treatments were further validated with relative work function values from Kelvin probe measurements. CBM energy level was calculated using the bandgap value of 1.84 eV for $CuGa_3Se_5$. For as deposited bulk thin films, $E_F - E_{VBM} = 0.28$ eV was calculated using the carrier concentration of $\sim 2 \times 10^{14}$ cm^{-3} from Hall effect measurement and the carrier effective masses were obtained from literature [39]. The attainable CBM range for MZO is from our previous combinatorial study [29].

An E_F–E_{VBM} of 0.55 eV for the as deposited absorber surface suggested a downward band bending with reduced p-type conductivity. A NH_4OH treatment lowered the value to 0.41 eV due to the removal of surface states. E_F–E_{VBM} increased to 0.6 eV with Cd^{2+} treatment, likely due to Cd replacing Cu, creating compensating defect(s) on the absorber surface. This implied a shift in surface conductivity type towards becoming intrinsic. Cadmium did not appear to dope the surface fully n-type, unlike what was reported for CIGSe or CISe [40, 41]. CIGSe and CISe normally are p-type at the surface and after cation exchange with cadmium solution, become n-type. However, Cd^{2+} treatment for $CuGa_3Se_5$ only moved the Fermi level upward, closer to being intrinsic.

3.4. Photovoltaic characterization

To understand the influence of the contact CB position on the absorber performance in PEC environment, MZO with varying composition was integrated with $CuGa_3Se_5$ absorbers into solid state test structures with top TCO and metal contacts. For the baseline PV device ($CuGa_3Se_5$/CdS/i-ZnO material stack), the open circuit voltage (V_{OC}) = 730 mV, short-circuit current (J_{SC}) = 5.7 mA cm^{-2}, fill factor (FF) = 61%, and efficiency 2.6% were achieved. Initial devices with CdS contact layer, and MZO layer replacing i-ZnO layer showed promising results: V_{OC} = 755 mV, J_{SC} = 7.6 mA cm^{-2}, FF = 38.4%, and efficiency 2.1% (supplementary figure S5). A clear CdS layer was observed in SEM (figure 6(a)), STEM/HAADF (figure 6(c)) and STEM/EDX (figure 6(e)) images.

MZO was then studied as a replacement for the CdS/i-ZnO contact stack. PV devices without any surface treatment of the as-deposited $CuGa_3Se_5$ did not exhibit any quantifiable current generation. Solution treatments of $CuGa_3Se_5$ indicated a pathway to replace CdS with MZO, with MZO grown directly on NH_4OH-treated and Cd^{2+} solution treated $CuGa_3Se_5$ surfaces. The NH_4OH treatment of the absorber prior to MZO deposition resulted in some PV activity, although the device performance values were quite low. Cd^{2+} solution treated $CuGa_3Se_5$ surfaces led to improved PV performance, and some incorporation of Cd into $CuGa_3Se_5$ surfaces.

The material stack for the PV devices with 65 °C Cd-treated $CuGa_3Se_5$ absorbers and MZO contacts are shown in figure 6(b). The effect of the Cd^{2+} solution treatment could not be resolved from the SEM

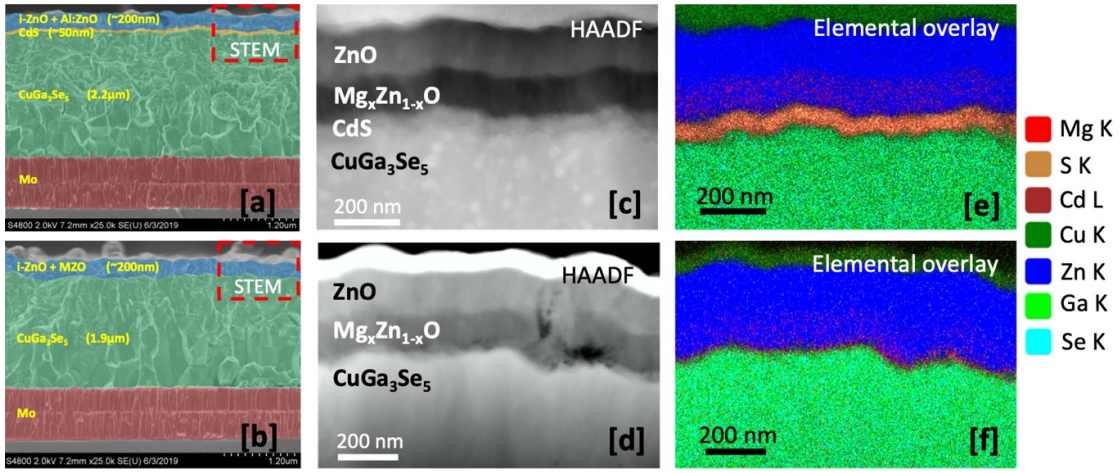

Figure 6. Microscopy images of $CuGa_3Se_5$/MZO devices with (a), (c), (e) CdS, and interfaces with (b), (d), (f) Cd^{2+} solution treatment, including (a), (b) SEM images with color overlay for the PV devices, (c), (d) STEM HAADF images and (e), (f) STEM EDX elemental maps at the $CuGa_3Se_5$/MZO interfaces.

Table 3. Photovoltaic device performance for different configurations. The values with bold font indicate highest achieved parameters.

Device configuration	V_{OC} (mV)	J_{SC} (mA cm^{-2})	FF (%)	Efficiency (%)
CGS/CdS/i-ZnO	730	5.7	**61.4**	**2.6**
CGS/CdS/MZO	755	7.6	38.4	2.1
CGS/Cd^{2+} 65 °C 14 min/MZO	**925**	4.8	41.9	1.9
CGS/Cd^{2+} 85 °C 7 min/MZO	650	**8.3**	47.6	**2.6**

(figure 6(b)) or STEM/HAADF (figure 6(d)) images, indicating that very small amount of Cd was substituted at the surface (as indicated by XPS). However, STEM/EDX elemental map of the device revealed Cd present at the $CuGa_3Se_5$/MZO interface (figure 6(f)). Elemental line profiles from STEM/EDX showing the change in elemental composition across the cross section for these devices is shown in supplementary figure S6. A small amount of sulphur (S) is also present at this interface, which is likely due to $CdSO_4$ that was the source of Cd^{2+}.

The device performances were dependent on the temperature and the duration of the Cd^{2+} treatment (figure 7). Lower treatment temperature (65 °C 15 min) improved the open circuit voltage, with the highest V_{OC} of 925 mV for Mg composition of $x = 10.8\%$ in MZO. For this treatment, Cd mostly remained at the interface (TEM data) and the surface Fermi level was moved towards intrinsic (XPS data). Higher temperature treatment could cause Cd to diffuse further to reduce p-type conductivity in the bulk $CuGa_3Se_5$ absorber. Cd^{2+} treatment at 85 °C 7 min resulted in higher J_{SC} up to 8.3 mA cm^{-2} (figure 7(c) and table 3), however with a reduced V_{OC}. Lower hole concentration in the bulk absorber would extend the depletion region causing improved carrier collection at longer wavelengths (QE data, figure 7(b)). Lowering of the bulk p-type conductivity would also lower the device V_{OC}, as observed in this case. Cu deficient surface and grain boundary assisted Cd diffusion is reported in many literatures during chemical bath deposition (CBD) of CdS on similar polycrystalline chalcopyrites, such as $CuGaSe_2$ [42], CIGSe [43, 44], and $CuInSe_2$ [45]. Same chemicals as CdS CBD were used for Cd^{2+} treatment, excluding the S source. Such diffusion in Cu-deficient ordered vacancy chalcopyrite $CuGa_3Se_5$ could be even more dominant [46].

Comparing QE of different device configurations (figure 7(b)) showed that replacing CdS with MZO improved the carrier collection in the short wavelengths due to the higher bandgap of MZO. As shown previously, the conductivity of MZO could be improved by doping with Ga, which required higher substrate temperature. However, device performance was significantly reduced with V_{OC} in the range of 400–500 mV and many devices with doped MZO were shunted (data not shown), possibly due to the higher temperature exposure.

The PV device performance for various configurations are summarized in table 3. Although significant open-circuit voltage improvement was observed in MZO based devices, the FF and photocurrent output were reduced. The $CuGa_3Se_5$/(Cd^{2+})/MZO PV devices had superior open-circuit voltage of 925 mV compared to 730–755 mV for CdS based devices, likely due to the combined effect of favorable CB offset and surface passivation by Cd^{2+} treatment. Besides, the thin Cd containing layer on the $CuGa_3Se_5$ surface could have a protective effect against bombardment of the sputtering ions on the absorber during MZO growth.

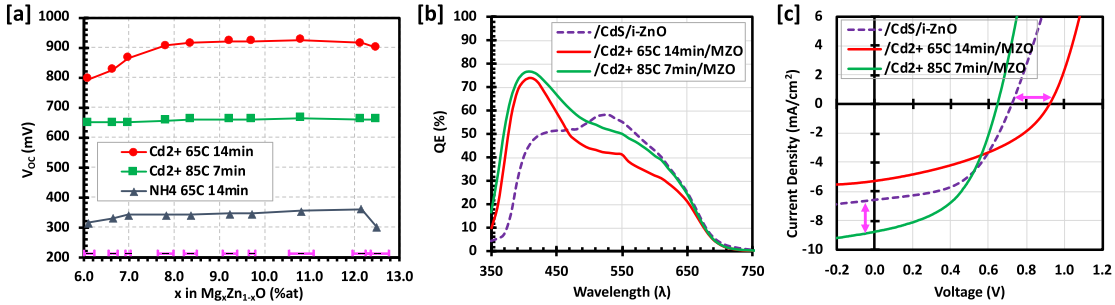

Figure 7. PV performance for CdS-free $CuGa_3Se_5/Mg_xZn_{1-x}O$ devices with different surface treatments, including (a) open circuit voltage, (b) external quantum efficiency, and (c) current voltage characteristics. The magenta bars at the bottom axis of panel (a) represent standard errors in each Mg composition.

Looking at the complete device structure, $CuGa_3Se_5/(Cd^{2+})$/MZO/Al:ZnO/metal grid, the n-type counterpart for the p-type $CuGa_3Se_5$ absorber in this case is likely MZO/Al:ZnO bilayer. Change of absorber surface conductivity type to either intrinsic or slightly n-type could create a better p–i–n junction that improved the device V_{OC}, where bulk of the $CuGa_3Se_5$ absorber is the p-type layer, the MZO/Al:ZnO is the n-type bilayer stack, and the Cd^{2+}-treated $CuGa_3Se_5$ surface is the intrinsic (i) layer.

MZO contacted $CuGa_3Se_5$ absorber PV device data fulfilled two important requirements for top cell tandem device application: high V_{OC} and improved QE in the blue region of the spectrum. Although direct water splitting tests were not performed yet due to the instability of MZO in acidic solutions, LSV testing in sacrificial redox couple showed promising outcomes. A thin protective layer deposited on top of MZO could improve stability and facilitate water splitting experiments, like demonstrated for bare CGS surfaces [47]. More experiments are in progress to integrate such protective coatings on MZO without degrading underlying absorber/contact interface, and will be reported in the future.

4. Conclusion

MZO contact integration with $CuGa_3Se_5$ absorber has been demonstrated. MZO deposition and absorber surface treatment parameters are determined for improved PV device performance, which allowed the elimination of the CdS contact layer. Characterization of the $CuGa_3Se_5$ films with Cd^{2+} solution surface treatment indicated that the beneficial effect of the treatment is due to removal of surface oxidation and change in surface doping by Cd substitution. The PEC characteristics of the devices were promising for future water splitting applications: from linear sweep voltammetry in 10 mM hexaammineruthenium (III) chloride, a photocurrent onset potential near 1 V vs RHE was observed. For solid state PV devices, replacing CdS/i-ZnO with MZO improved the carrier collection in the short wavelengths and resulted in open circuit voltage of 925 mV, which is promising for top-cell tandem PV device applications. The results of this research will facilitate the understanding of $CuGa_3Se_5$/MZO interface, and the use of $CuGa_3Se_5$ absorbers for both PEC and PV device applications.

Acknowledgments

This work was authored in part by the National Renewable Energy Laboratory (NREL), operated by Alliance for Sustainable Energy LLC, for the U.S. Department of Energy (DOE) under contract no. DE-AC36-08GO28308. Funding provided by the Office of Energy Efficiency and Renewable Energy (EERE), under 'Hydrogen and Fuel Cell Technologies Office (HFTO)', as a part of HydroGEN Energy Materials Network (EMN) consortium project administrated by the University of Hawaii under contract no. DE-EE0006670. The authors would like to acknowledge John Perkins and Bobby To of NREL for the RBS analysis and SEM images respectively. The views expressed in the article do not necessarily represent the views of the DOE or the U.S. Government.

ORCID iDs

Imran S Khan https://orcid.org/0000-0002-8483-2896
Christopher P Muzzillo https://orcid.org/0000-0002-6492-0098
Andriy Zakutayev https://orcid.org/0000-0002-3054-5525

References

[1] Christopher K and Dimitrios R 2012 A review on exergy comparison of hydrogen production methods from renewable energy sources *Energy Environ. Sci.* **5** 6640–51
[2] Fujishima A and Honda K 1972 Electrochemical photolysis of water at a semiconductor electrode *Nature* **238** 37–38
[3] Miller E L, Marsen B, Paluselli D and Rocheleau R 2005 Optimization of hybrid photoelectrodes for solar water-splitting *Electrochem. Solid-State Lett.* **8** 247–9
[4] Cheng W H *et al* 2018 Monolithic photoelectrochemical device for direct water splitting with 19% efficiency *ACS Energy Lett.* **3** 1795–800
[5] Gaillard N, Prasher D, Kaneshiro J, Mallory S and Chong M 2013 Development of chalcogenide thin film materials for photoelectrochemical hydrogen production *MRS Proc.* **1558** mrss13-1558-z02-07
[6] Moriya M, Minegishi T, Kumagai H, Katayama M, Kubota J and Domen K 2013 Stable hydrogen evolution from CdS-modified $CuGaSe_2$ photoelectrode under visible-light irradiation *J. Am. Chem. Soc.* **135** 3733–5
[7] Zhang L, Minegishi T, Kubota J and Domen K 2014 Hydrogen evolution from water using $Ag_xCu_{1-x}GaSe_2$ photocathodes under visible light *Phys. Chem. Chem. Phys.* **16** 6167–74
[8] Zhang L *et al* 2015 Durable hydrogen evolution from water driven by sunlight using (Ag,Cu)GaSe2 photocathodes modified with CdS and CuGa3Se5 *Chem. Sci.* **6** 894–901
[9] Deangelis A D, Horsley K and Gaillard N 2018 Wide band gap $CuGa(S,Se)_2$ thin films on transparent conductive fluorinated tin oxide substrates as photocathode candidates for tandem water splitting devices *J. Phys. Chem.* C **122** 14304–12
[10] Gaillard N *et al* 2019 Wide-bandgap $Cu(In,Ga)S_2$ photocathodes integrated on transparent conductive $F:SnO_2$ substrates for chalcopyrite-based water splitting tandem devices *ACS Appl. Energy Mater.* **2** 5515–24
[11] Muzzillo C P *et al* 2018 Low-cost, efficient, and durable H_2 production by photoelectrochemical water splitting with $CuGa_3Se_5$ photocathodes *ACS Appl. Mater. Interfaces* **10** 19573–9
[12] Zhang S B, Wei S-H and Zunger A 1997 Stabilization of ternary compounds via ordered arrays of defect pairs *Phys. Rev. Lett.* **78** 4059–62
[13] Kim J, Minegishi T, Kobota J and Domen K 2012 Investigation of Cu-deficient copper gallium selenide thin film as a photocathode for photoelectrochemical water splitting *Japan. J. Appl. Phys.* **51** 1–6
[14] Seitz L C, Chen Z, Forman A J, Pinaud B A, Benck J D and Jaramillo T F 2014 Modeling practical performance limits of photoelectrochemical water splitting based on the current state of materials research *ChemSusChem* **7** 1372–85
[15] Kim J, Minegishi T, Kobota J and Domen K 2012 Enhanced photoelectrochemical properties of $CuGa_3Se_5$ thin films for water splitting by the hydrogen mediated co-evaporation method *Energy Environ. Sci.* **5** 6368–74
[16] Kumagai H, Minegishi T, Moriya Y, Kubota J and Domen K 2014 Photoelectrochemical hydrogen evolution from water using copper gallium selenide electrodes prepared by a particle transfer method *J. Phys. Chem.* C **118** 16386–92
[17] Siebentritt S and Rau U (eds) 2006 *Wide-Gap Chalcopyrites* (Berlin: Springer)
[18] Ruckh M, Schmid D and Schock H W 1994 Photoemission studies of the ZnO/CdS interface *J. Appl. Phys.* **76** 5945–8
[19] Weinhardt L, Heske C, Umbach E, Niesen T P, Visbeck S and Karg F 2004 Band alignment at the i-ZnO/CdS interface in $Cu(In,Ga)(S,Se)_2$ thin-film solar cells *Appl. Phys. Lett.* **84** 3175–7
[20] Zhang S B, Wei S-H and Zunger A 1998 A phenomenological model for systematization and prediction of doping limits in II–VI and I–III–VI_2 compounds *J. Appl. Phys.* **83** 3192–6
[21] Gloeckler M and Sites J R 2005 Efficiency limitations for wide-band-gap chalcopyrite solar cells *Thin Solid Films* **480–481** 241–5
[22] Song T, Kanevce A and Sites J R 2016 Emitter/absorber interface of CdTe solar cells *J. Appl. Phys.* **119** 233104
[23] Minemoto T *et al* 2001 Theoretical analysis of the effect of conduction band offset of window/CIS layers on performance of CIS solar cells using device simulation *Sol. Energy Mater. Sol. Cells* **67** 83–88
[24] Minemoto T, Negami T, Nishiwaki S, Takakura H and Hamakawa Y 2000 Preparation of $Zn_{1-x}Mg_xO$ films by radio frequency magnetron sputtering *Thin Solid Films* **372** 173–6
[25] Ohtomo A *et al* 1998 $Mg_xZn_{1-x}O$ as a II-VI widegap semiconductor alloy *Appl. Phys. Lett.* **72** 2466–8
[26] Takeuchi I *et al* 2003 Monolithic multichannel ultraviolet detector arrays and continuous phase evolution in $Mg_xZn_{1-x}O$ composition spreads *J. Appl. Phys.* **94** 7336–40
[27] Bendersky L A, Takeuchi I, Chang K-S, Yang W, Hullavarad S and Vispute R D 2005 Microstructural study of epitaxial Zn1-xMg xO composition spreads *J. Appl. Phys.* **98** 083526
[28] Lautenschlaeger S, Sann J, Klar P J, Piechotka M and Meyer B K 2009 Combinatorial growth of MgxZn1-xO epilayers by chemical vapor deposition *Phys. Status Solidi* B **246** 383–6
[29] Rajbhandari P P, Bikowski A, Perkins J D, Dhakal T P and Zakutayev A 2017 Combinatorial sputtering of Ga-doped (Zn,Mg)O for contact applications in solar cells *Sol. Energy Mater. Sol. Cells* **159** 219–26
[30] Ablekim T, Colegrove E and Metzger W K 2018 Interface engineering for 25% CdTe solar cells *ACS Appl. Energy Mater.* **1** 5135–9
[31] Chantana J, Kato T, Sugimoto H and Minemoto T 2018 20% efficient $Zn_{0.9}Mg_{0.1}O:Al/Zn_{0.8}Mg_{0.2}O/Cu(In,Ga)(S,Se)_2$ solar cell prepared by all-dry process through a combination of heat-light-soaking and light-soaking processes *ACS Appl. Mater. Interfaces* **10** 11361–8
[32] Minemoto T, Hashimoto Y, Satoh T, Negami T, Takakura H and Hamakawa Y 2001 $Cu(In,Ga)Se_2$ solar cells with controlled conduction band offset of window/$Cu(In,Ga)Se_2$ layers *J. Appl. Phys.* **89** 8327–30
[33] Hultqvist A, Platzer-Björkman C, Pettersson J, Törndahl T and Edoff M 2009 $CuGaSe_2$ solar cells using atomic layer deposited Zn(O,S) and (Zn,Mg)O buffer layers *Thin Solid Films* **517** 2305–8
[34] Talley K R *et al* 2019 COMBIgor: data-analysis package for combinatorial materials science *ACS Comb. Sci.* **21** 537–47
[35] Zakutayev A *et al* 2018 An open experimental database for exploring inorganic materials *Sci. Data* **5** 1–12
[36] Contreras M A *et al* High efficiency $Cu(In,Ga)Se_2$-based solar cells: processing of novel absorber structures *Conf. Record of the IEEE Photovoltaic Specialists Conf.* vol 1 pp 68–75
[37] Bard A and Faulkner L 2020 *Electrochemical Methods, Fundamentals and Applications* 2nd edn (New York: Wiley)
[38] Reese M O *et al* 2015 Intrinsic surface passivation of CdTe *J. Appl. Phys.* **118** 155305
[39] Marín G, Rincón C, Wasim S M, Sánchez Pérez G and Molina I 1999 Temperature dependence of the fundamental absorption edge in $CuGa_3Se_5$ *J. Alloys Compd.* **283** 1–4
[40] Hunger R *et al* 2005 SXPS investigation of the Cd partial electrolyte treatment of CuInSe2 absorbers *Thin Solid Films* **480–481** 218–23
[41] Han J-F *et al* 2014 TEM and XPS studies on CdS/CIGS interfaces *J. Phys. Chem. Solids* **75** 1279–83

[42] Rusu M et al 2009 Three-dimensional structure of the buffer/absorber interface in CdS/ $CuGaSe_2$ based thin film solar cells *Appl. Phys. Lett.* **95** 173502
[43] Nakada T and Kunioka A 1999 Direct evidence of Cd diffusion into $Cu(In,Ga)Se_2$ thin films during chemical-bath deposition process of CdS films *Appl. Phys. Lett.* **74** 2444–6
[44] Nakada T 2000 Nano-structural investigations on Cd-doping into $Cu(In,Ga)Se_2$ thin films by chemical bath deposition process *Thin Solid Films* **361** 346–52
[45] Ramanathan K et al 2009 Junction formation in CuInSe2-based thin-film devices *AIP Conf. Proc.* **462** 9–16
[46] Kiss J, Gruhn T, Roma G and Felser C 2013 Theoretical study on the diffusion mechanism of Cd in the Cu-poor phase of CuInSe2 solar cell material *J. Phys. Chem.* C **117** 25933–8
[47] Palm D W, Muzzillo C P, Ben-Naim M, Khan I, Gaillard N and Jaramillo T F 2021 Tungsten oxide-coated copper gallium selenide sustains long-term solar hydrogen evolution *Sustain. Energy Fuels* Advance Article (https://doi.org/10.1039/d0se00487a)